Supporting Information:

Fluorine-Rich Schiff Base Ligand Derived Fe/N-C-F and Co/N-C-F Catalysts for Oxygen Reduction Reaction: Synthesis, Experimental Validation, and DFT Insights

Sumanta Kumar Das[†a,b], Shaik Gouse Peera[†c], Aiswarya Kesh[a], Prabakaran Varathana[a,b], and Akhila Kumar Sahu[a,b*]

[a]CSIR - Central Electrochemical Research Institute - Madras Unit, CSIR Madras Complex, Taramani, Chennai - 600 113, India.

[b]Academy of Scientific and Innovative Research (AcSIR), Ghaziabad-201 002, India.

[c]*Natural Science Research Institute, College of Natural Sciences, Keimyung University, 1095, Dalseo-gu, Daegu 42601, Republic of Korea*

*To whom correspondence should be addressed, E-mail: aksahu@cecri.res.in (A. K. Sahu)

† Both authors contributed Equally

This Supplementary Material includes: Contents

Section S1 Experimental section

2.1 Chemicals

Salicylaldehyde, 98% and Pentafluorophenylhydrazine, 97% were procured from Sigma-Aldrich. Iron precursor [Iron (III) chloride, 98%, pure, anhydrous] and Cobalt precursor [Cobalt (II) Chloride Hexahydrate extra pure AR, 99%] and solvents like Ethanol 99.9%; Toluene, ACS, 99.5% and glacial acetic acid were procured from Alfa Aesar, Mumbai, India. All the specified chemicals were of analytical grade and were employed as-is without any additional refinement. The deionized water (DI) used in all experiments was produced by a Millipore system and had a resistivity of about 18.2 MΩ cm.

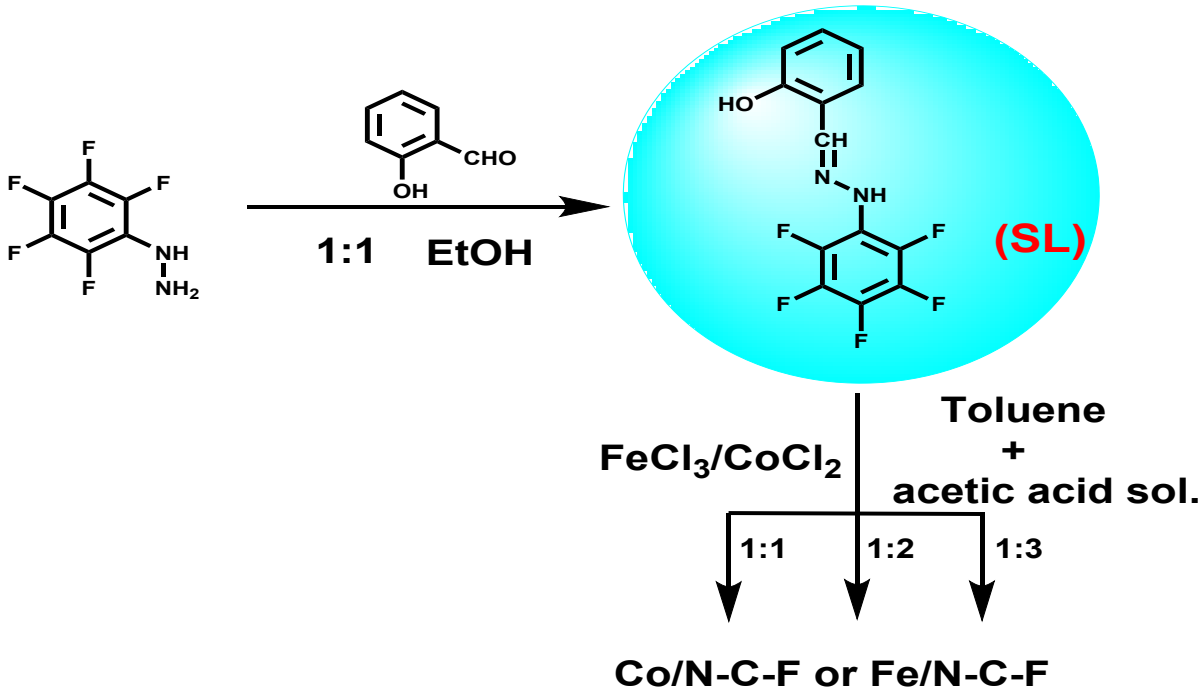

Scheme S1: Schematic illustrations of the synthesis process of Schiff base Ligand (SL) and the formation of metal coordinated complex Fe/N-C-F and Co/N-C-F.

Section S2 Instruments and Physicochemical characterizations

1H NMR: Proton Nuclear Magnetic Resonance spectra were obtained at 298 K in CDCl3 using a BRUKER Advance (400 MHz) spectrometer, providing insights into the specific bonding structure and stereochemistry of the organic molecules.

XRD: The BRUKER D8 Advance diffractometer was utilized for non-destructive X-ray diffraction (XRD) measurements, yielding precise information about the crystallographic structure, physical, and chemical properties of the synthesized metal-doped ligand. Measurements were conducted at 1.5405 Å using Cu–Kα as the X-ray source, with a 2θ range of 10-80° and a scan rate of 10° min^{-1}.

BET: Surface geometry was governed via Brunauer-Emmett-Teller (BET) equation and Pore Size Distribution (PSD) curve was procured by the Barrett-Joyner-Halenda (BJH) method. Patternable and textural geometry of heteroatom doped catalyst were outlined by N_2 adsorption-desorption isotherms, well thought out at 77K using Quanta chrome Autosorb® iQ-MP / iQ-XR.

Raman Spectroscopy: Raman spectroscopy (RFS27, BRUKER) employing an Nd: YAG laser at a wavelength of 1064 nm was deliberately used to evaluate the metals (Fe, Co) doped on the ligand framework and study the defect chemistry associated with it.

TEM: Morphological characterization of the prepared material was performed using a Transmission Electron Microscopy (TEM, Tecnai 20 G2 instrument, 80 keV to 200 keV) to determine particle size, shape, and atomic arrangements at localized regions within the materials with a take-off angle close to 0 degrees, to maximize the interaction between the electron beam and the specimen.

SEM: The microstructural evaluation of the Metal-Organic Framework (MOF) in relation to metal doping was investigated using Scanning Electron Microscopes (SEM, FEI Quanta FEG 200).

XPS: X-ray Photoelectron Spectroscopy (XPS) studies were carried out using an ESCALAB 250 XPS system (Thermo Fisher Scientific) with a monochromatic Al Kα source at 15 keV and 150 W. This analysis allowed the chemical state of elements (primarily their binding energies) to be determined, along with understanding the active arrangement of heteroatoms in the catalyst. The binding energy of each element in the catalysts was calibrated by using the C1s peak located at 284.6 eV as a reference.

Section S3 Electrochemical Measurements

ORR Measurements

Electrochemical investigations were carried out using a potentiostat/galvanostat (Biologic instruments, VSP/VMP 3B-20) at 30 °C. A standard three-electrode system was employed, consisting of a Hg/HgO reference electrode, a glassy carbon (GC) working electrode, and a graphite rod counter electrode. The GC electrode surface was smoothened with 0.3 μm alumina powder and then ultrasonically rinsed in a mixture of deionized water and ethanol. The catalyst ink was prepared by mixing 1 mL of ethanol and water (1:1 ratio), 10 μL of Nafion ionomer (binder), and 5 mg of the prepared catalyst. The catalyst ink was sonicated to obtain the desired consistency and then dropped onto the GC electrode, achieving a catalyst loading of approximately 500 μg cm^{-2}. All potentials mentioned are changed and reported with regard to RHE throughout the study, unless stated differently.

The current density in the electrochemical experiments was determined by dividing the measured current by the geometric area of the glassy carbon electrode (GCE). To make the potential values consistent and comparable across different experiments, the potential versus the HgO/Hg reference electrode was converted to the potential relative to the reversible hydrogen electrode (RHE) using the following formula[4]:

$$E_{vs\ RHE} = E_{vs\ HgO/Hg} + E^{\theta}_{HgO/Hg}(0.0978\ V) + 0.0592\ pH \quad (1)$$

Here, $E_{vs\ RHE}$ refers to the potential relative to the RHE, which serves as a standardized reference for comparing and analyzing the electrochemical data. $E_{vs\ HgO/Hg}$ represents the potential measured against the HgO/Hg reference electrode, while $E^{\theta}_{HgO/Hg}$ denotes the standard electrode potential of the HgO/Hg electrode.

The conversion equation incorporates a correction factor (0.0978 V) based on the standard electrode potential of the HgO/Hg electrode, which ensures a consistent reference potential across different measurements. Additionally, the pH value of the electrolyte is considered by adding the term 0.0592 pH, further accounting for the electrochemical conditions.

By applying this conversion, the electrochemical data can be uniformly expressed relative to the RHE, allowing for accurate comparisons and interpretations of the experimental results. This standardized approach is crucial for understanding the behavior of the studied electrochemical systems and drawing meaningful conclusions from the obtained data.

Cyclic voltammograms (CVs) and linear sweep voltammograms (LSVs) were recorded in 0.1 M aqueous KOH electrolyte to investigate the electrochemical behaviour of the catalysts. The CVs were recorded within a potential window of 0.2 to -0.8 V (vs. saturated calomel electrode) at a scan rate of 20 mV s^{-1} in O_2–saturated electrolyte. The LSVs were performed in O_2–saturated electrolyte using 0.1 M KOH solution at a rotation speed of 1600 rpm to determine the onset potential and kinetics, such as half-wave potential ($E_{1/2}$), kinetic current density (ik), and limiting currents (iL). To verify the number of electrons transferred during the process, hydrodynamic voltammograms were recorded at various rotational speeds (800, 1200, 1600, 2000, and 2400 rpm) in O_2–saturated 0.1 M KOH at a scan rate of 5 mV s^{-1}, using the K–L plot method. Additionally, the K−L plots serve as a graphical representation of the total electron transport (n) involved in ORR process and are calculated using kinetic equations 2 and 3.

$$\frac{1}{j} = \frac{1}{j_k} + \frac{1}{j_L} \qquad (2)$$

$$= \frac{1}{j_k} + \frac{1}{B\omega^{1/2}} \qquad (3)$$

Where 'j' corresponds to measured current density, 'j_K' represents kinetic current density, 'j_L' signifies diffusion-limiting current density, 'ω' is angular velocity measured in radians per second (rad s^{-1}), and 'B' is a parameter derived from equation 4 that follows

$$B = 0.62\, nFC_{O_2}(D_{O_2})^{2/3}\nu^{-1/6} \quad (4)$$

In the above equation, 'n' represents number of electrons transferred per molecule of O_2, 'F' is the value for Faraday's constant (96,485 C mol^{-1}), 'C_{O2}' indicates concentration of oxygen in electrolyte (1.2×10^{-6} mol cm^{-3}), 'D_{O2}' is the diffusion coefficient of oxygen in solution (1.9×10^{-5} cm^2 s^{-1}), and 'υ' denotes kinematic viscosity of 0.1 M aqueous KOH electrolyte (0.01 cm^2 s^{-1}). The magnitude and similarity observed in K-L plots within potential range of 0.2 to –0.8 V suggest that reaction kinetics follow a first-order reaction with respect to concentration of dissolved O_2.

The electrochemical durability of the catalyst in an alkaline environment was assessed by conducting repeated CVs up to 20000 potential cycles for both F Fe/N-C-F and Co/N-C-F catalysts. The deterioration mechanism of the catalysts during the durability cycles was compared with the LSVs data obtained after 20000 repeated potential cycles.

Furthermore, the ORR process related to the percentage peroxide yield and the number of electrons transferred was verified through Rotating Ring-Disk Electrode (RRDE) experiments. Saturated calomel electrode (SCE) and graphite rod were used as reference and counter electrodes, respectively. Pine Instruments were used to perform the RRDE experiments, utilizing a 5 mm GC disk and a Pt ring with a diameter of 5.5. The RRDE working electrode was prepared by dropping 10 μL of the formulated catalyst dispersed mixture, which was air-dried at room temperature before analysis. . In addition to parameters mentioned earlier, RRDE analysis was performed to validate ORR pathway, calculate total electron transfer, and measure HO_2^- yield of catalysts using subsequent equation 5,

$$H_2O_2 = 200 \times \frac{I_r/N}{I_d + I_r/N} \quad (5)$$

$$n = 2 \times \frac{2I_d}{I_d + I_r/N} \quad (6)$$

Within this context, 'N' signifies the current-capturing capacity of the Pt ring, 'I_r' designates the ring current, and 'I_d' is the term for the disk current. These comprehensive electrochemical characterizations provide valuable insights into the catalytic performance and stability of Fe/N-C-F and Co/N-C-F catalysts for potential applications in anion exchange fuel cells.

Section S4. Membrane electrode assembly (MEA) fabrication and AEM fuel cell performance evaluation

Performance analysation in anion exchange fuel cell (AEFC) was accomplished employing the standard testing protocols and using optimized Fe/N-C-F and Co/N-C-F as cathode catalysts to carry MEA fabrication. For both anode and cathode, the commercially available gas diffusion layers (GDL, SGL BC–39) were chosen. A slurry was prepared dispersing both the prepared catalyst individually in ethanol for a while and then adding the 10 wt. % Fumion FAA-3 ionomer in sequence with continuous sonication for 30 min. Conventional brush coating technique was adopted on GDL to achieve ~0.5 mg cm^{-2} catalyst loading at cathode. On the other hand, the anode side was coated with commercial Pt/C (20 wt. %) to obtain a loading of 0.5 mg cm^{-2}. A MEA was assembled by inserting an anion exchange membrane between the electrodes and pressing them at 85 °C and at the pressure of 20 kg cm^{-2}. Prior to pressing, both the electrodes were drenched in 1 M aqueous KOH solution for about 12 h for the exchange of the Br^- ions from ionomer to OH^- ion present in the solution under ambient conditions. For anion exchange membrane the commercial Fumatech membranes of 50 μm thickness were used. The membrane was initially treated with 2 M aqueous KOH at room temperature for 48 h so as to replace Cl^- ions in the membrane with OH^- ions in the solution which was further used while fabricating MEA[5]. The prepared MEA, graphite plates with a parallel serpentine flow field all were coupled together in fuel cell text fixtures (Fuel cell Tech. Inc., USA) of 5 cm^2 active area. Maximum relative humidity was maintained inside the cell while purging gaseous H_2 and O_2 into anode and cathode side of the cell respectively at a flow rate of ~200 mL min^{-1} through bubble humidifiers. The AEFC performance tests and

Galvanostatic polarization studies were conducted by using Fuel cell test station (Fuel Cell Technologies Inc., N3300A) at 45.

S5. DFT (Density Functional Theory) studies

DFT (Density Functional Theory) calculations of catalytic cycle reveal the underlying reasons for superior ORR performance of Fe/N-C-F catalyst when compared to Co/N-C-F. All modeling and optimization tasks were performed using the DFT method with the B3LYP function and 6-31G* basis set, utilizing Gaussian 09 software. The presence of solvent (water) was considered in calculations using the self-consistent reaction field (SCRF) model, and models were constructed with fragments of graphene to explore its catalytic properties, particularly focusing on the arrangement of metal atoms enclosed by nitrogen atoms within a system of conjugated aromatic rings. The reactions 7a, 7b, and 8 represent the ORR scheme in an alkaline solution.

$$O_2(g) \rightarrow O_2(ads) \overset{H_2O}{\rightarrow} OOH\,(ads) + OH^- \rightarrow OOH^- + OH^- \quad (7a)$$

$$O_2(g) \rightarrow O_2\,(ads) \overset{H_2O}{\rightarrow} OOH\,(ads) + OH^- \rightarrow O\,(ads) + 2OH^- \overset{H_2O}{\rightarrow} OH\,(ads) + 3OH^- \rightarrow 4\,OH^-$$

(7b)

$$O_2(g) \rightarrow O_2\,(ads) \rightarrow O\,(ads) + O\,(ads) \overset{2H_2O}{\rightarrow} 2OH\,(ads) + 2OH^- \rightarrow 4OH^- \quad (8)$$

The primary mechanism selected for specific active center was four-electron reduction associative mechanism 7b. Subsequently, the chosen intermediates played a crucial role in modeling process.

1) $O_2 + 2H_2O$
2) $O_{2(ads)} + 2H_2O$
3) $OOH_{(ads)} + H_2O + OH^-$

4) $O_{(ads)} + H_2O + 2OH^-$
5) $OH_{(ads)} + 3OH^-$
6) $4OH^-$

Gibbs free energy was utilized with an electron energy correction that accounted for thermal free energy, in order to compare the energies of optimized structures, which is calculated as follows.

$$G = E_{ele} + E_{ZPE} + E_{therm} + k_B T - TS_{tot} \quad (9)$$

Where, the provided equation involves multiple variables, E_{ele} (total electronic and nuclear repulsion energy at 0 K), E_{ZPE} (zero-point vibrational energy), E_{therm} (total thermal internal energy), k_B (Boltzmann's constant), S_{tot} (system entropy), and T (temperature, specifically T = 298.15 K).

$$E_{therm} = E_t + E_r + E_v + E_e \quad (10)$$

Where Ef_t represents the thermal internal energy resulting from translational motion, E_r corresponds to internal energy originating from rotational motion, E_v denotes the internal energy associated with vibrational motion, and E_e stands for internal energy attributed to electronic motion. The reference point for energy calculations was established by summing energies of final optimized substances and catalyst, effectively setting it as zero level. Adsorption energy was then computed employing the following formula

$$G_{ads} = G_{system} - G_{adsorbate} - G_{catalyst} \quad (11)$$

To assess energy implications of continuing processes, we have identified following elementary reactions taking place at catalyst's surface.

Section S6 Figures and Tables

Electrochemical parameters at V versus RHE			
Catalyst type	**Mass activity (A/mg)**	**Specific activity (mA/cm^2)**	**Tafel slope ($mV\ dec^{-1}$)**
Fe/N-C-F	0.46	1.5	89
Co/N-C-F	0.41	1.3	87
$Pt_{20\%}/C$	0.54	1.6	77

Table S1. Comparison of iK, MA and Tafel slope of Fe/N-C-F, Co/N-C-F and commercial $Pt_{20\%}/C$ catalyst.

Catalyst types	**C**	**O**	**N**	**F**	**Fe**	**Co**
Co/N-C-F	60.22	30.16	3.61	0.91	-	5.1
Fe/N-C-F	58.07	29.03	4.49	0.97	7.44	-

Table S2. Comparison of elemental composition of Fe/N-C-F and Co/N-C-F catalysts.

Table S3. Comparison of Results with State-of-the-Art Literature**.**

S. No.	Heteroatoms and metals in the catalyst	Electrolyte KOH or $HClO_4$	#Onset/*halfwave potential V vs. RHE	#Fuel cell/ *Zn-Air performance mW cm^{-2}	Ref. No
1	N, F, Fe on carbon (corn cob)	KOH	*0.92	#38	69
2	Fe, N on CNFs	KOH	*0.89	*96.6	9
3	Fe, N, P on CNTs	KOH	*0.88	*145	18
4	Fe, N, P on carbon (COF)	KOH & $HClO_4$	*0.89 & *0.75	-	19
5	Fe-NF on CNTs	KOH	#0.90/*0.85	#144	17
6	N,F,C@Fe/Fe3C-9	KOH	#0.99/ *0.87	#96	17
7	N,F-Co&CoN@C700	KOH	#0.92/ *0.87	-	17
8	Co/NSF-C700	KOH	#0.98/ *0.80	-	17
9	Fe–Co/NF–GNF	KOH	#0.93/*0.77	-	17
10	Co/PCNF	KOH	#0.87/*0.78	-	17
11	Tri(Fe/N/F)-doped MCNFs	KOH	#0.90/*0.82	-	17
12	FeNFC800	KOH	#0.95/*0.82	#196	17
13	F-FeNC	KOH	#0.91/*0.82	#141	17
14	Co, N on ZIF-8	KOH	*0.87	*110	20
15	**Fe, N, F On Caron (Schiff base metal complex)**	**KOH**	***0.88**	**#75**	**Present work**

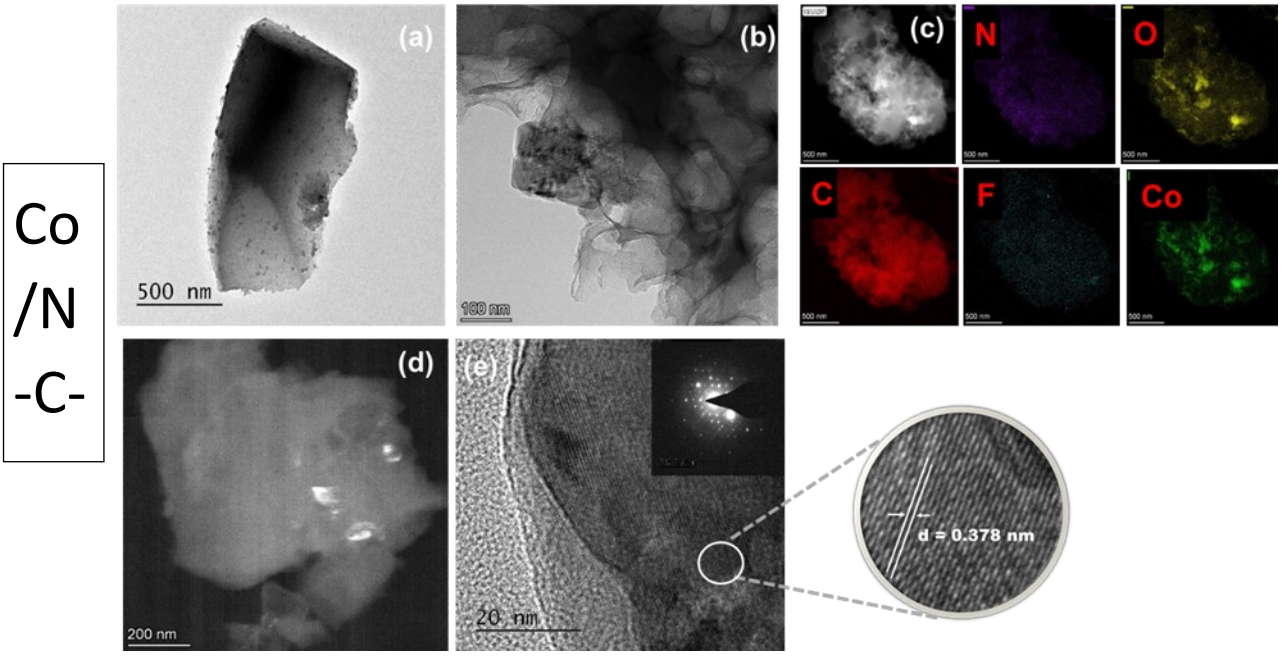

Fig. S1 TEM images of (a,b) Co/N-C-F (c) HR-TEM images of Co/N-C-F (The corresponding selected area diffraction patterns are shown in insets, lattice fringes details given).

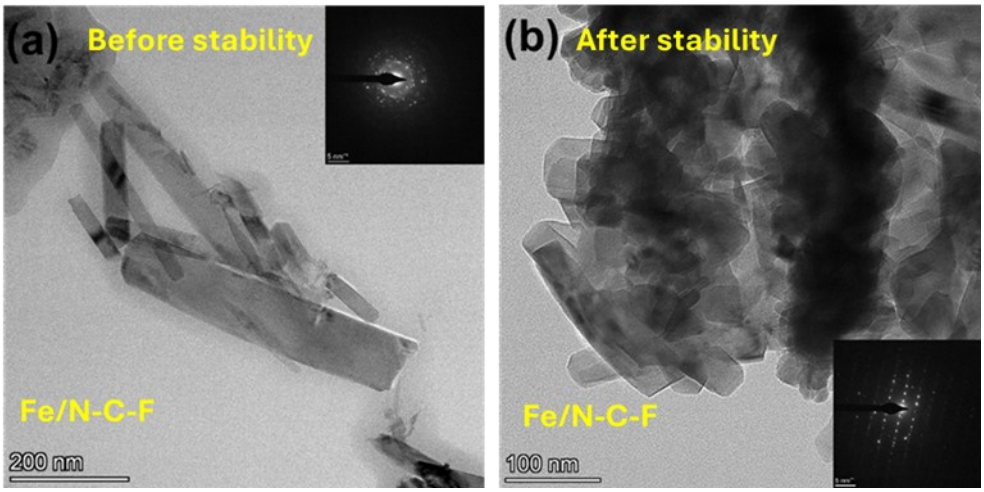

Fig. S2 Microstructure analysis of Fe/N-C-F (a) before and (b) after 20000 cycling tests.

(i)

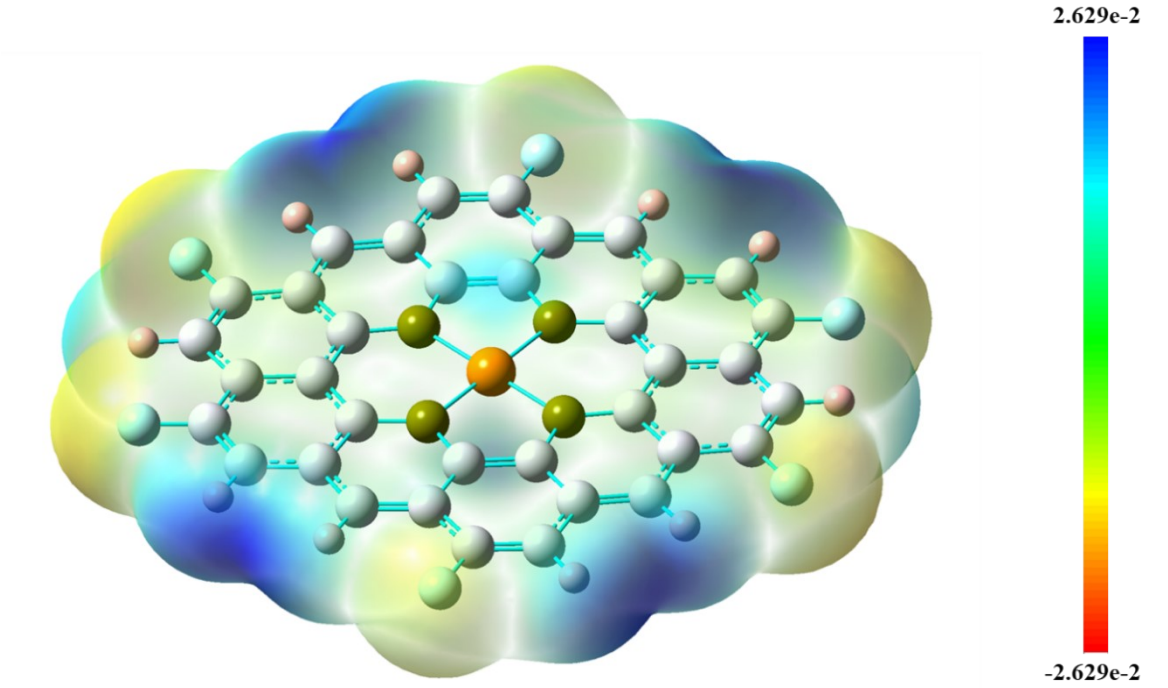

(ii)

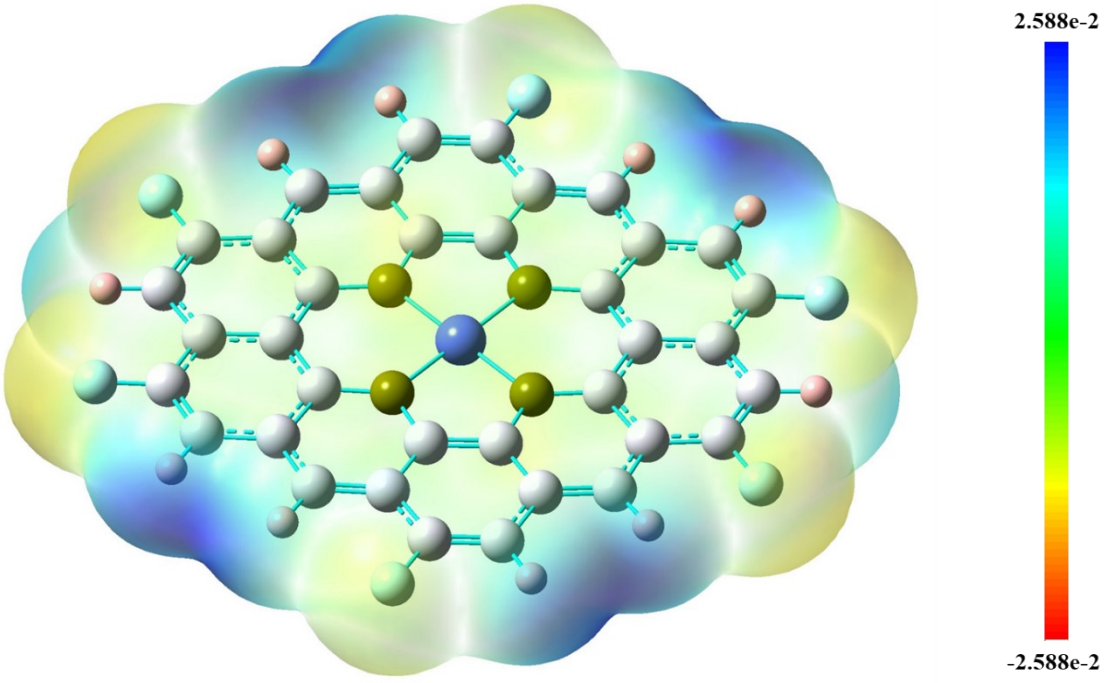

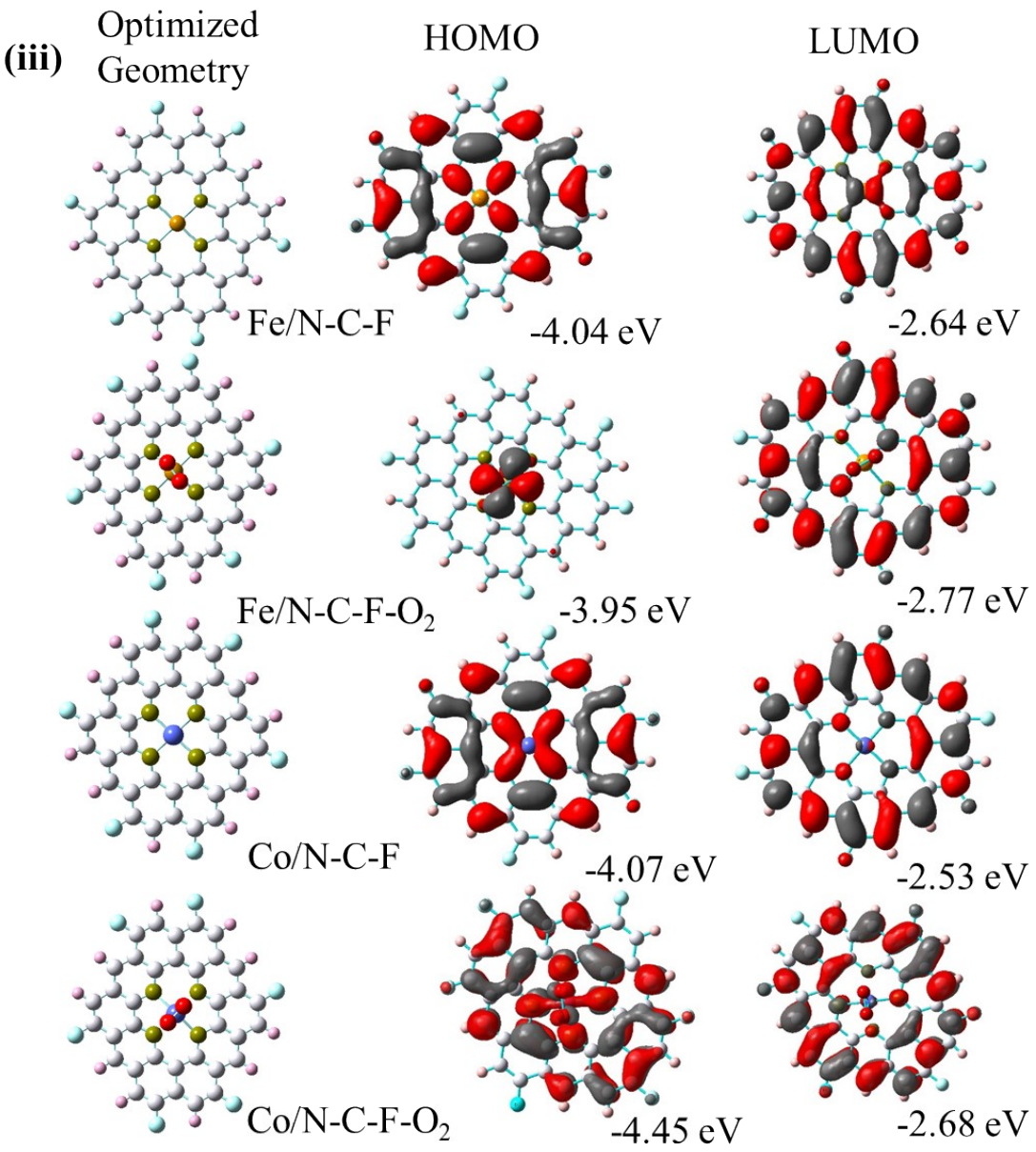
(iii)
Optimized Geometry
HOMO
LUMO
Fe/N-C-F
-4.04 eV
-2.64 eV
Fe/N-C-F-O2
-3.95 eV
-2.77 eV
Co/N-C-F
-4.07 eV
-2.53 eV
Co/N-C-F-O2
-4.45 eV
-2.68 eV

(iv)

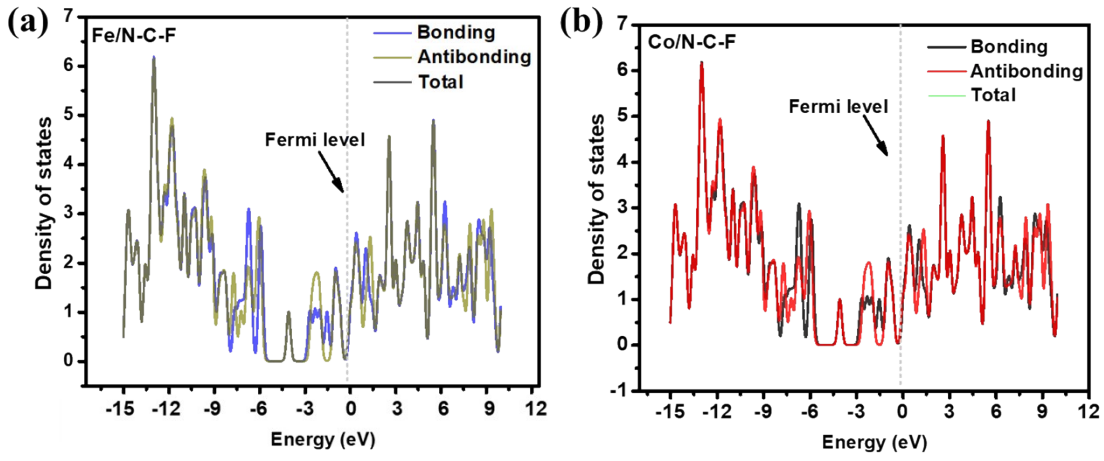
(a)
Fe/N-C-F
Bonding
Antibonding
Total
Fermi level
Density of states
Energy (eV)
(b)
Co/N-C-F
Bonding
Antibonding
Total
Fermi level
Density of states
Energy (eV)

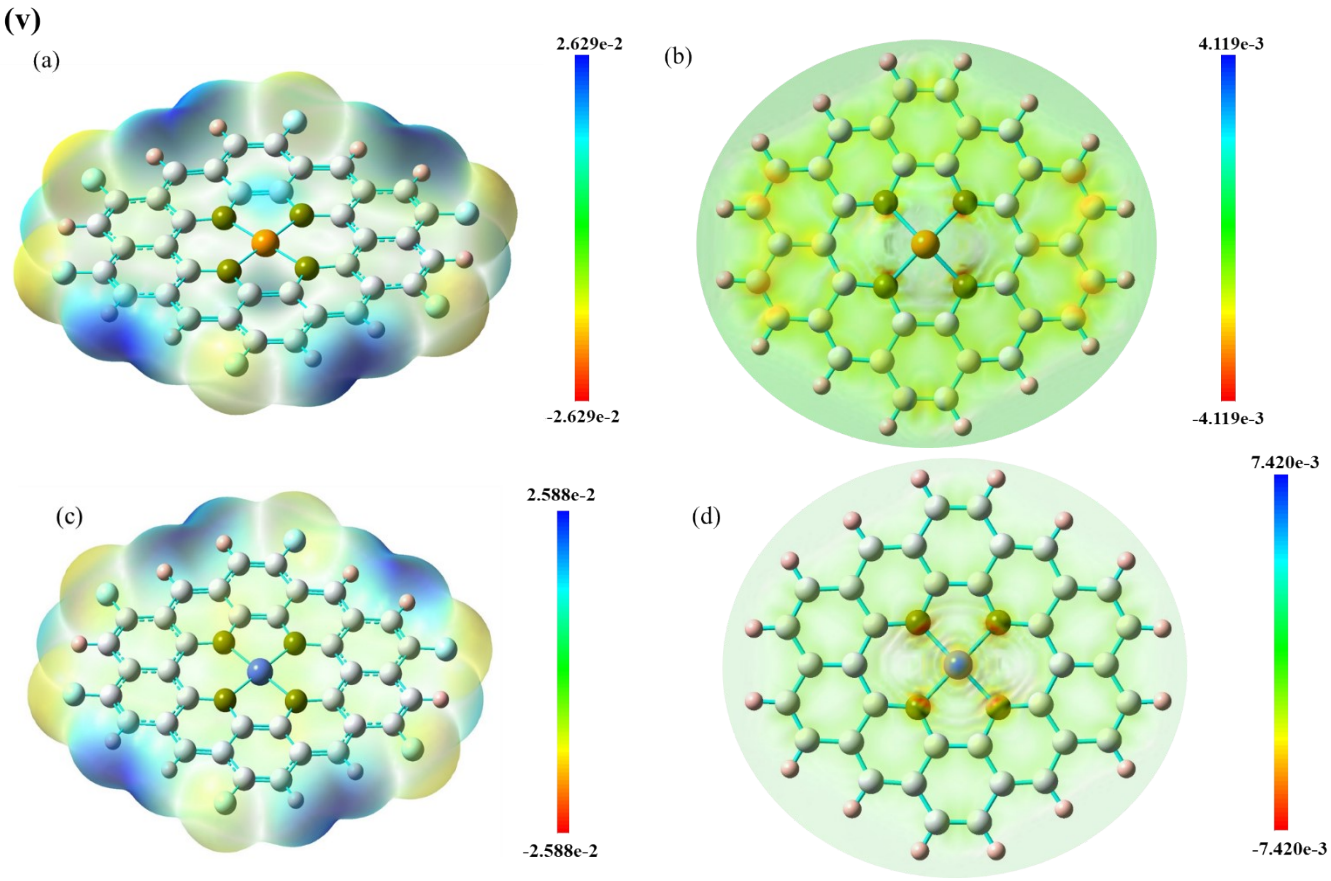

Fig. S3. Molecular electrostatic potential (MEP) mapped surface of (i) Fe/N-C-F, (ii) Co/N-C-F calculated at an isovalue of 0.0004, representing the electrostatic potential. (iii) Atomic orbital compositions of frontier molecular orbitals and optimized geometries of Fe/N-C-F, Fe/N-C-F-O_2, Co/N-C-F and Co/N-C-F-O_2. The presence of red colored charge clouds in the molecule indicates the presence of positive ion whereas negative ion is indicated as grey. (iv) PDOS of (a) Fe/N-C-F, (b) Co/N-C-F (v) Comparisons of Charge cloud difference of (a, b) Fe/N-C and (c, d) Co/N-C catalyst.

In the MEP mapping analysis, the visualization of the positive charge cloud (depicted in blue color) reveals that the M center (metal center) in the case of Fe (Fe/N-C-F) exhibits a higher degree of activity compared to Co (Co/N-C-F). This observation is supported by the fact that the positive charge cloud is more pronounced around Fe of Fe/N-C-F catalyst, indicating a stronger electrostatic interaction and higher reactivity at the M center for Fe. Conversely, the positive charge cloud around Co in Co/N-C-F catalyst appears to be less intense, suggesting relatively lower reactivity at the Co M center. These findings are illustrated in **Fig. S3**, providing valuable insights into the relative catalytic activities of Fe and Co in the studied system. The atomic orbital compositions of frontier molecular orbitals and optimized

geometries of Fe/N-C-F, Fe/N-C-F-O_2, Co/N-C-F, and Co/N-C-F-O_2 catalysts are shown in **Fig. S3 (iii)**. The red-colored charge clouds in the molecule represent the presence of positive ions, while the grey charge clouds indicate negative ions. In the Fe/N-C-F structure, the red charge clouds are primarily concentrated around the Fe centers, suggesting positively charged ORR active sites that promote O_2 adsorption. Upon O_2 binding (Fe/N-C-F-O_2), these charge clouds increase around the metal centers, indicating enhanced ORR activity. On the other hand, in the Co/N-C-F structure, the Co centers display red charge clouds, and the charge density decreases in Co/N-C-F-O_2, demonstrating a comparatively lower concentration of ORR active centers due to metal-ion interaction with the adsorbed oxygen molecule. In catalytic ORR, the adsorption of O_2 onto the catalytic surface is the rate-determining step, as it requires a significant amount of energy to initiate the reaction. This calculations reveals that the Fe/N-C-F catalyst exhibits a lower energy barrier for O_2 adsorption compared to the Co/N-C-F catalyst. This indicates that the Fe/N-C-F catalyst facilitates stronger and more stable adsorption of the O_2 molecule onto its active sites, which is a crucial factor in the ORR process. The presence of a well-optimized coordination environment in the Fe/N-C-F catalyst, likely due to the Fe-N4 moieties, enhances its ability to bind oxygen molecules more effectively than Co/N-C-F.

The PDOS plots compare the bonding and antibonding interactions of Fe/N-C-F (left) and Co/N-C-F (right) catalysts as shown in **Fig. S3 (iv)**. In the Fe/N-C-F system, the bonding states (blue) are more pronounced below the Fermi level (0 eV), indicating stronger and more stable interactions. Antibonding states (yellow) are minimal near the Fermi level, suggesting higher catalytic stability. In contrast, the Co/N-C-F system shows a greater presence of antibonding states, indicating weaker stability. This suggests that Fe/N-C-F has superior catalytic performance for ORR compared to Co/N-C-F.

Moreover, in DFT calculations comparing Fe/N-C and Co/N-C catalysts, fluorine (F) doping significantly alters charge distribution. As shown in **Fig. S3 (v)** without F doping, the positive charge concentrates on the metal atom, limiting active sites for the ORR. In contrast, F doping delocalizes the positive charge, creating multiple active centers that enhance catalytic performance. Both F-doped Co/N-C and Fe/N-C catalysts demonstrate improved ORR activity compared to their undoped counterparts. This suggests that F doping is beneficial for developing more efficient fuel cell catalysts.

Table S4: Calculation of bond distance between metal atom – oxygen bond distance, Oxygen – oxygen bond distance and oxygen – hydrogen bond distance.

Bond Distance	Fe/N-C-F (in Å)			Co/N-C-F (in Å)		
	Fe – O	**O – O**	**O – H**	**Co – O**	**O – O**	**O – H**
Cat. + $O_{2(ads)}$	1.84	1.39	---	1.80	1.37	---
Cat. + $OOH_{(ads)}$	1.76	1.45	0.97	1.74	1.43	0.97
Cat. + $O_{(ads)}$	1.70	---	---	1.67	---	---
Cat. + $OH_{(ads)}$	1.90	---	0.97	1.84	---	0.97
Cat. + OH^-	1.99	---	0.96	1.94	---	0.96

Section S7 References

References:

[1] M. Shaabani, Synthesis and characterization of cobalt complexes with pentafluorophenylhydrazine : Nucleophilic attack of phenolic oxygen to pentafluorophenyl ring during condensation of two Schiff base ligands, 160 (2014) 34–40. https://doi.org/10.1016/j.jfluchem.2014.01.013.

[2] X. Liu, J. Hamon, Recent developments in penta- , hexa- and heptadentate Schiff base ligands and their metal complexes, Coord. Chem. Rev. 389 (2019) 94–118. https://doi.org/10.1016/j.ccr.2019.03.010.

[3] M. Cazacu, S. Shova, A. Soroceanu, P. Machata, L. Bucinsky, M. Breza, P. Rapta, J. Telser, J. Krzystek, V.B. Arion, Spectroelectrochemistry, and Theoretical CalculationsCharge and Spin States in Schi ff Base Metal Complexes with a Disiloxane Unit Exhibiting a Strong Noninnocent Ligand Character: Synthesis, Structure, (2015). https://doi.org/10.1021/acs.inorgchem.5b00229.

[4] J. Zhang, Z. Mei, L. Yi, J. Tian, K. Li, X. Hu, Y. Zhang, R. Wang, H. Guo, S. Zang, Applied Catalysis B : Environmental Highly accessible and stable Co-based active sites enabled by 2D / 3D dual-confined strategy for Zn-air batteries, 338 (2023).

[5] S. Akula, A.K. Sahu, Structurally modulated graphitic carbon nanofiber and heteroatom (N,F) engineering toward metal-free ORR electrocatalysts for polymer electrolyte membrane fuel cells, ACS Appl. Mater. Interfaces. 12 (2020) 11438–11449. https://doi.org/10.1021/acsami.9b18790.